EUMETSAT Satellite Application Facility on Climate Monitoring

Visiting Scientist Report

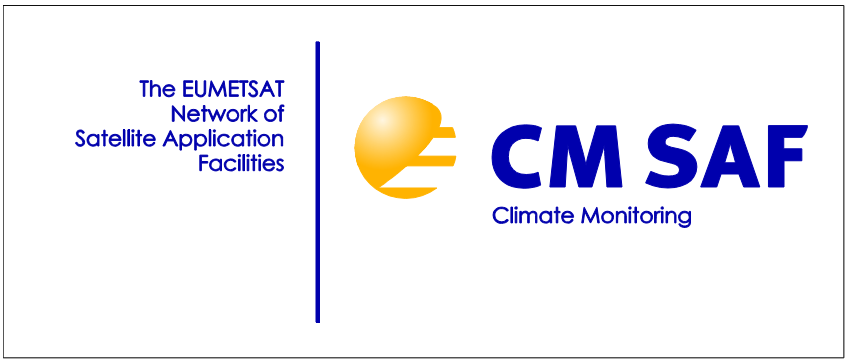

Studying aerosol indirect effects by combining CM-SAF cloud microphysical property data with NO_2 retrievals

CDOP VS Study No 22

Date **14.2.2012**

Studying aerosol indirect effects by combining CM-SAF cloud microphysical property data with NO_2 retrievals (CMSAF_CDOP_KNMI_AS22)

Ruud Dirksen, Jan Fokke Meirink

14 February 2012

Abstract

In this study the correlation between OMI tropospheric NO_2 and cloud physical parameters was investigated, motivated by the idea to use OMI NO_2 as a proxy for AOT in observing the aerosol indirect effect. OMI NO_2 observations were compared to MODIS AOT and cloud physical parameters from SEVIRI and PATMOS-x over Europe, Africa and China. No clear correlation is found in the daily observations, but for monthly averaged measurements higher NO_2 values correspond to smaller SEVIRI r_e over eastern Europe and the Po-valley, the decrease of r_e levels off for NO_2 columns exceeding 3×10^{15} molecules/cm^2. Over China and selected biomass burning regions in Africa higher NO_2 values correlate with smaller monthly averaged r_e observations from PATMOS-x, although in case of Africa this relation can also result from climatology as biomass burning predominantly occurs in summer.

1 Introduction

Twomey (1974) proposed that aerosol emitted by anthropogenic activities increases the number of available cloud condensation nuclei (CCN), resulting in more and smaller cloud droplets than would be the case in an aerosol-lean environment. This change of cloud properties due to air pollution was dubbed the aerosol indirect effect (AIE). The AIE influences the Earth's radiation budget as decreasing droplet size increases the cloud's albedo, which makes it relevant for climate change, although the magnitude of the radiative forcing by the AIE is highly uncertain and it is currently estimated at –0.7 W/m^2 (*IPCC*, 2007).

A considerable amount of research effort has been devoted to observing and modeling of the aerosol indirect effect. Satellite observations reveal changes of cloud physical parameters leeward of major continents as was shown using MODIS (*Bennartz*, 2007) and PATMOS-x (*Rausch et al.*, 2010). Furthermore, a trend analysis shows an increase of cloud droplet size and a suppression of precipitation over the China Sea resulting from the increasing pollution

in China (*Bennartz et al.*, 2011). These studies have in common that the aerosol indirect effect is found in long-term observations over large areas, which is an indication that it may be cumbersome to observe the AIE on a local scale from space. A nice example of the observation of the AIE on a local scale was the cloud-formation in ship exhaust plumes (*Twohy et al.*, 1995). *Brenguier and Wood* (2009) discuss the difficulties involved in discerning the –relatively small– changes in cloud properties that are induced by the AIE from the changes resulting from the natural variability and dynamics of the weather/climate system. Therefore, the optimal case for observing the AIE is an area which exhibits stable meteorological conditions over a prolonged period, such that the only varying parameter is the atmospheric aerosol load. For this reason most studies involving space borne observations of AIE focused on (sub)-tropical oceanic regions that are characterized by persistent strato-cumulus cloud cover.
Another complicating factor in the spaceborn observation of AIE is the fact that satellite observations of aerosol optical thickness (AOT) with instruments like MODIS is restricted to cloud-free scenes, which hampers the simultaneous retrieval of aerosol load and cloud physical parameters which is needed to investigate the AIE. The goal of this project is to investigate the feasibility to use tropospheric NO_2 measurements from the Ozone Monitoring Instrument (OMI) as a proxy for the aerosol load in studying the AIE in SEVIRI observations, which is inspired by the fact that

- tropospheric NO_2 columns can readily be retrieved over cloudy scenes, although the retrieval is insensitive to below-cloud NO_2 (*Boersma et al.*, 2004).
- *Veefkind et al.* (2011) reported a correlation between MODIS AOT and OMI tropospheric NO_2 columns.

Using NO_2 as a proxy for (anthropogenic) aerosol constitutes an adaptation of the approach employed by *Avey et al.* (2007) who used CO as a passive tracer in the analysis of MODIS data.
Primarily, this study was focused on Europe, but as no clear AIE signature was found, this study was expanded to include PATMOS-x observations over Africa and southeast Asia as well. The lack of a clear AIE signal over Europe is attributed to the naturally occurring large variability in cloud properties due to regularly passing low pressure systems which is typical for the climate in temperate zones. In addition, PATMOS-x observations are available from 1982 onwards, whereas the SEVIRI dataset used in this study is limited to a 12-month period in 2008–2009.

2 Methodology & data sets

In this study spaceborne observations of tropospheric NO_2, AOT and cloud physical parameters from various satellite instruments were used; the origin and properties of the respective data sets are listed in Table 1. The time window was chosen based on the availability of OMI data (from October 2004 onwards) and SEVIRI data (a 12-month period from June 2008 to May 2009).

OMI, SEVIRI and PATMOS-x (daily) data were interpolated to a common rectangular grid (0.25°x0.25°), MODIS AOT data and PATMOS-x monthly averages were already available at a 1°x1° grid. Additional filtering/screening for clouds was performed as indicated in Table 1. Sections 2.2–2.5 provide a more detailed discussion of the data treatment. Analyses were performed on the daily data sets and on monthly averages that were constructed from the daily data; the results are presented in (scatter)density plots, and time series of the data.

2.1 Regions of interest

Table 2 lists the regions of interest used in this study. These regions are located in Europe, Africa, and east-Asia. The regions in Europe are loosely based on the regions used by *Veefkind et al.* (2011) and coincide with known industrialized areas with elevated tropospheric NO_2 levels. The general circulation pattern over mid-latitude Europe is characterized by predominantly western winds that transport relatively clean air masses with low tropospheric NO_2 content from the Atlantic Ocean. The majority of the CCNs in the air over the Atlantic Ocean are of natural origin (sea spray), although occasionally long range transport of pollution from the American continent makes it all the way across the Atlantic Ocean. Nevertheless, the region over the eastern Atlantic represents the unpolluted reference case.
The regions R_2–R_5 coincide with major seasonal biomass burning areas in Africa. R_0, R_6 and R_7 lie in the main outflow regions that receive aerosols from the African continent (see, e.g., *Staudt et al.* (2002); *Edwards et al.* (2006)). Region R_1 represents the clean background case over the southern Atlantic ocean.
In East Asia the highly industrialized region around Shanghai is selected together with its outflow area over the China Sea.

Table 1: Overview of regridded data products used in this study.

Instrument	Data product	Resolution		Region	Selection criteria	Time range	Reference
		Spatial (°x°)	Temporal				
OMI	DOMINO trop. NO_2	0.25x0.25	Daily	Global	all data	2005–2009	*Boersma et al.* (2007)
MODIS	AOT	1x1	Daily	Global	Cloud-free	2005–2009	*Tanré et al.* (1997)
SEVIRI		0.25x0.25	15 minutes	Europe	Rule 1*	06/2008–05/2009	*Roebeling et al.* (2006)
PATMOS-x		1x1	Monthly	Global	all data	2005–2009	*Rausch et al.* (2010)
PATMOS-x		0.1x0.1	Daily	Africa	all data	2005–2009	*Rausch et al.* (2010)

*Selection rule: fully clouded pixels, liquid cloud phase, COD $>$8.

2.2 OMI

Tropospheric NO_2 columns were retrieved from OMI observations by the DOAS-based DOMINO algorithm (*Boersma et al.*, 2007). All available data were used, i.e., no filtering based on cloud fraction was applied. The OMI level 2 data, with pixel sizes ranging from 13x24km^2 at nadir to approximately 13x100km^2 at the edge of the swath, were regridded to 0.25°x0.25° spatial

Table 2: Overview of geographic regions of interest used in this study. See Figure 1 for a graphical representation.

Region	Coordinates		Shortname
	Lat	Lon	
Eastern Atlantic ocean	45°–55°N	10°–20°W	EAO
UK	50°–55°N	5°W–2°E	UK
Western Europe	47°–54°N	2°–8°E	WE
Eastern Europe	45°–55°N	15°–30°E	EA
Benelux+Germany	50°–55°N	3°–8°E	BG
Po-valley	43°–46°N	7°–14°E	Po
China	28°–38°N	110°–12°0E	Ch
China Sea	25°–30°N	123°–128°E	ChS
R_0	10°S–3°N	5°W–8°N	R_0
R_1	20°–30°S	5°–13°E	R_1
R_2	0°–10°S	15°–25°E	R_2
R_3	5°–15°N	20°–30°E	R_3
R_4	6°–11°N	0°–10°W	R_4
R_5	20°–28°S	24°–32°E	R_5
R_6	4°–10°S	41°–50°E	R_6
R_7	26°–35°S	33°–40°E	R_7

resolution. OMI is in a polar, sun-synchronous orbit, with local equator crossing time of approximately 13h40. Due to its 2600 km wide swath global daily coverage is achieved, typically in 14.5 orbits (*Levelt et al.*, 2006). Tropospheric NO_2 columns can be retrieved for cloud-free and for cloudy scenes, although in the latter case screening by the clouds prevents detection of the below-cloud part of the column.

2.3 SEVIRI

From its geostationary orbit centered over the Greenwich meridian, the Spinning Enhanced Visible and Infrared Imager (SEVIRI) on board METEOSAT-9, records a spectrally resolved image of the Earth disc every 15 minutes. Cloud droplet size (r_e), Cloud optical depth (COD), liquid water path (LWP) and cloud droplet density (DNDV) are retrieved from the SEVIRI observations in the visible (600 nm) and near-infrared (1.6 μm) wavelength range using the algorithm described by *Roebeling et al.* (2006). For this study we used cloud physical parameter data processed locally at KNMI rather than the operational CM-SAF data, because the latter were processed with an older CPP version and are not based on optimally calibrated SEVIRI data for the time period of interest. Due to data processing considerations, the SEVIRI data used in this study were available from June 2008–May 2009 for an area roughly delimited by 30°–60°N and 30°W–50°E, where the northern boundary shifts with season. This area covers central Europe, north Africa and part of the eastern Atlantic ocean, as is illustrated in the left panel of Figure 2.

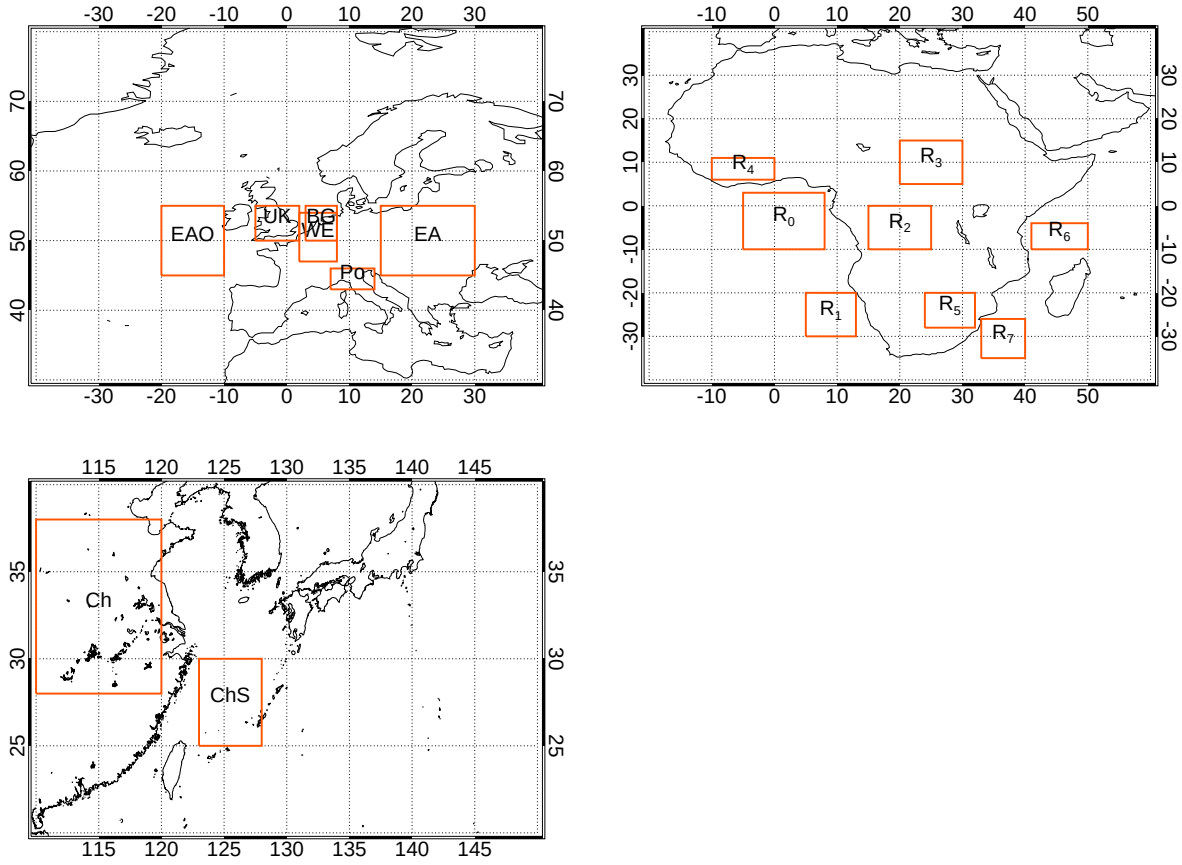

Figure 1: Maps showing the regions of interest listed in Table 2.

SEVIRIs spatial resolution ranges from 3x3 km^2 at nadir to 7x4 km^2 over central Europe. In this study, SEVIRI pixels are gridded to 0.25°x0.25°, where only those groundpixels are used that are completely covered with liquid water clouds with a COD larger than 8. The cloud-phase criterion restricts the data selection to clouds in the lower regions of the troposphere that are more likely to have interacted with aerosols, and the threshold value for the cloud optical depth excludes unreliable retrievals of cloud droplet size in optically thin clouds (*Roebeling et al.*, 2006).

2.4 MODIS

Spaceborn AOT observations from MODIS-AQUA were used. The AQUA spacecraft is part of NASA's A-train, so that MODIS-AQUA observes the same scene approximately 10 minutes prior to OMI. The daily 1°x1° gridded level 3 dataproduct was obtained from the Giovanni

website [1]. The following three products were downloaded: *Aerosol Optical Depth at 550 nm*, *Aerosol Optical Depth Pixel Counts*, *Cloud Fraction (Day only)*. The Aerosol Optical Depth Pixel Counts are necessary to construct weighted monthly averages from the daily AOT data, where cloud filtering was performed using the cloud fractions.

2.5 PATMOS-x

The Pathfinder Atmospheres-Extended (PATMOS-x) dataset is retrieved from observations by NOAA's Advanced Very High Resolution Radiometer (AVHRR). The goal of the PATMOS-x project is to derive atmospheric and surface climate records from AVHRR measurements that are available from 1982–present. In this study two kinds of PATMOS-x datasets were used; daily data taken over Africa, and monthly means of global observations. Both datasets comprise COD, r_e, and LWP. The daily data are available on a 0.1°x0.1° grid, whereas the global monthly means are provided on a 1°x1° grid. Similar to OMI and MODIS, AVHRR is in a polar orbit. As a result of that, the repetition rate of the PATMOS-x observations is much lower than for the geostationary SEVIRI instrument. Furthermore, considerable time differences occur between measurements taken over different regions, e.g., several hours between the eastern and the western part of the African continent. It is remarked that at the moment of writing the details regarding the data selection rules that were employed to construct the PATMOS-x monthly means used in this study are not known.

3 Results

3.1 OMI NO_2 versus SEVIRI & PATMOS-x cloud parameters

The map of the monthly mean value of tropospheric NO_2 over Europe, presented in Figure 3 shows a familiar spatial distribution, which is characterized by clearly distinguishable region with enhanced NO_2 over central Europe, stretching from the central UK to the eastern border of Poland. The industrialized regions in England, the Netherlands and the Ruhr area clearly stand out, as well as the Po valley in northern Italy.
When the NO_2 distribution of Figure 3 is compared to the to the map of SEVIRI r_e in Figure 2, some similarity is observed in the sense that r_e is smaller, and NO_2 is higher, over land than over the ocean, which shows a clear influence of the continent on both parameters. The smaller cloud droplet size over land is consistent with the inherently larger concentration of CCN in continental air. However, the distinct north-south gradient, which is apparent in the NO_2 distribution as elevated values confined roughly between 45–55°N latitude, is not clearly apparent in the r_e distribution. Yet, the reduction of SEVIRI r_e over Spain and southern France for the land-sea transistion is not as prominent as for the industrialized parts of Europe, which is consistent with the low NO_2 burden in these regions. This indicates that it is not that straightforward to find a correlation between NO_2 and the AIE from OMI and SEVIRI observations. Comparing

[1] http://gdata1.sci.gsfc.nasa.gov/daac-bin/G3/gui.cgi?instance_id=MODIS_DAILY_L3

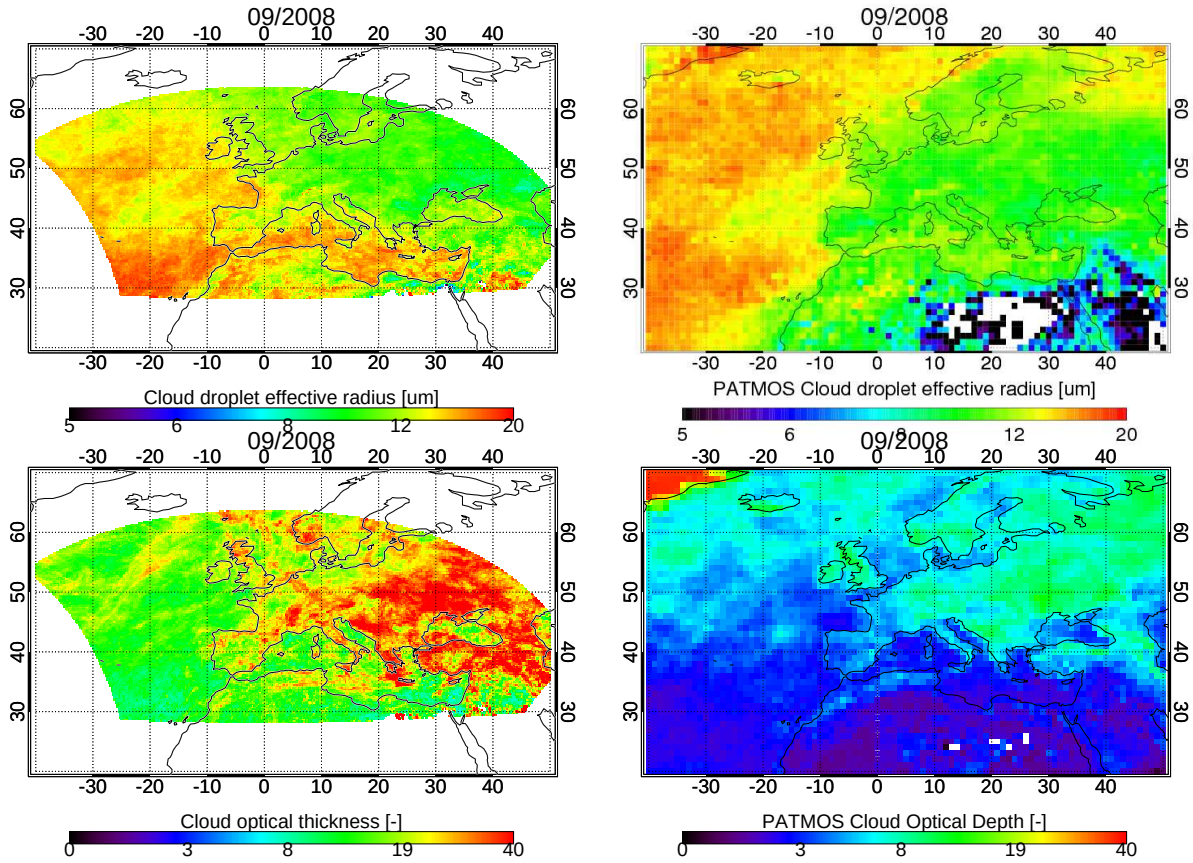

Figure 2: Maps of the monthly mean value of r_e over Europe for September 2008 as measured by SEVIRI (left) and PATMOS-x (right). The spatial patterns in r_e are to be compared to the distribution of tropospheric NO_2 shown in Figure 3. In all plots the applied color scale is logarithmic. Note that different selection criteria are applied between SEVIRI and PATMOS-x in constructing the monthly averages. This especially affects the monthly averaged COD, as in case of SEVIRI a threshold is applied, which results in higher COD values.

both maps in Figure 2 shows that SEVIRI and PATMOS-x observe similar distributions of cloud droplet size over Europe. Still, in comparison to SEVIRI the distribution of r_e derived from PATMOS-x is more uniform over the continent and smaller over the Mediterranean.
Over southern Africa, elevated NO_2 columns coincide with smaller r_e values, as can be seen in their respective spatial distributions for October 2008 that are presented in Figure 4. Yet, the question remains whether this spatial correlation between NO_2 and r_e is causal, or if both are connected by climatology, as biomass burning predominantly occurs in the dry season.

3.1.1 Scatter(density)plots

In the next step of the data analysis, the correlation between NO_2 and cloud parameters is investigated by means of scatter(density)plots. Figure 5 presents scatterdensity plots compiled of all grid points of the daily observations. These plots show no convincing correlation between

NO_2 and SEVIRI r_e: for NO_2 column values below 3×10^{15} molecules/cm^2 droplet sizes of 6–20μm more or less uniformly occur, without a clear trend between NO_2 and r_e. Yet, for the regions Europe and eastern Europe it is observed that for NO_2 columns exceeding 4×10^{15} molecules/cm^2, r_e tends to decrease with increasing NO_2, as is indicated by the red trace which represents the median of the r_e distribution.

Figure 6 presents scatterplots of regionally averaged monthly means of NO_2 and SEVIRI cloud parameters for Europe. Over the UK, western Europe and the Po-valley the COD increases with increasing NO_2 column, but over Eastern Europe such a trend can not clearly be identified due to the steady reduction of COD for NO_2 column values exceeding 5×10^{15} molecules/cm^2. Panel (b) of Figure 6 shows that the cloud droplet size decreases with increasing NO_2 burden over Eastern Europe and the Po-valley, while the decrease of r_e levels off for NO_2 columns exceeding 4×10^{15}molecules/cm^2. Yet, over the UK, western Europe and Benelux+Germany this relation between the monthly averages of NO_2 and cloud droplet size is, at best, tentative. Figure 7 presents scatterplots of collocated (gridded) monthly averages of NO_2 versus cloud

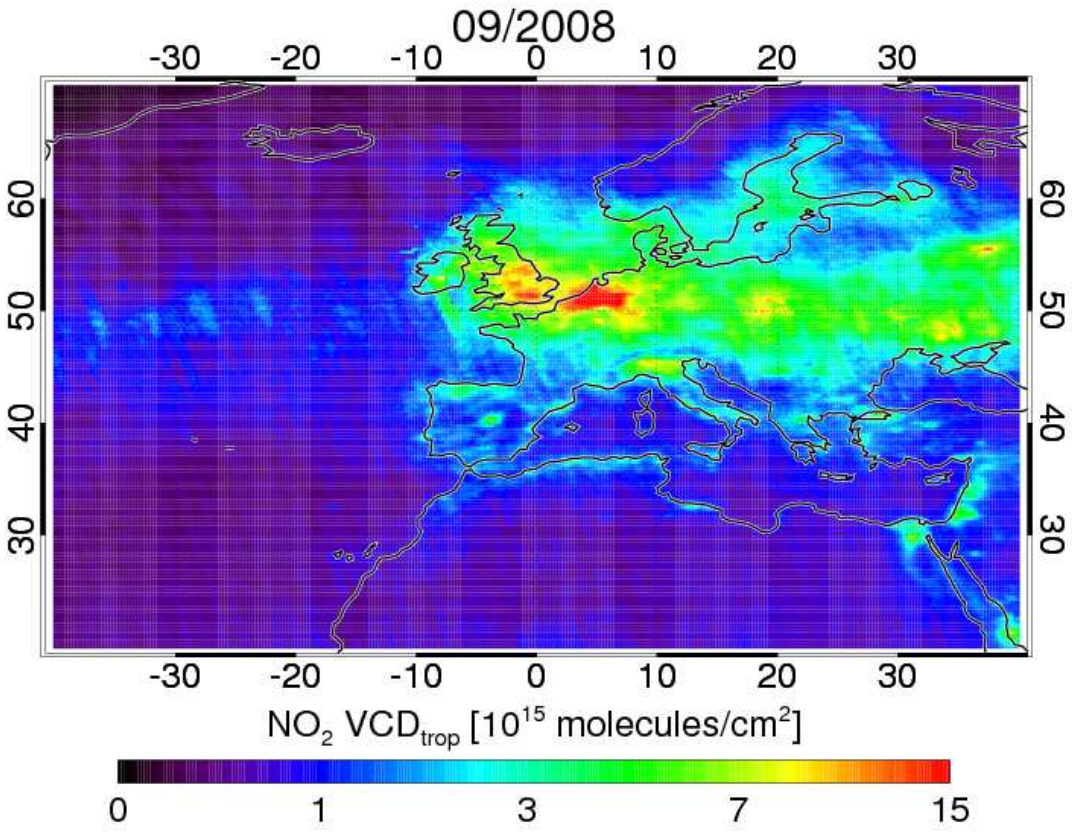

Figure 3: Monthly average of the OMI tropospheric NO_2 over Europe for September 2008. Note the logarithmic colorscale. Spatial patterns in the NO_2 distribution are to be compared to the distributions of cloud physical parameters presented in Figure 2.

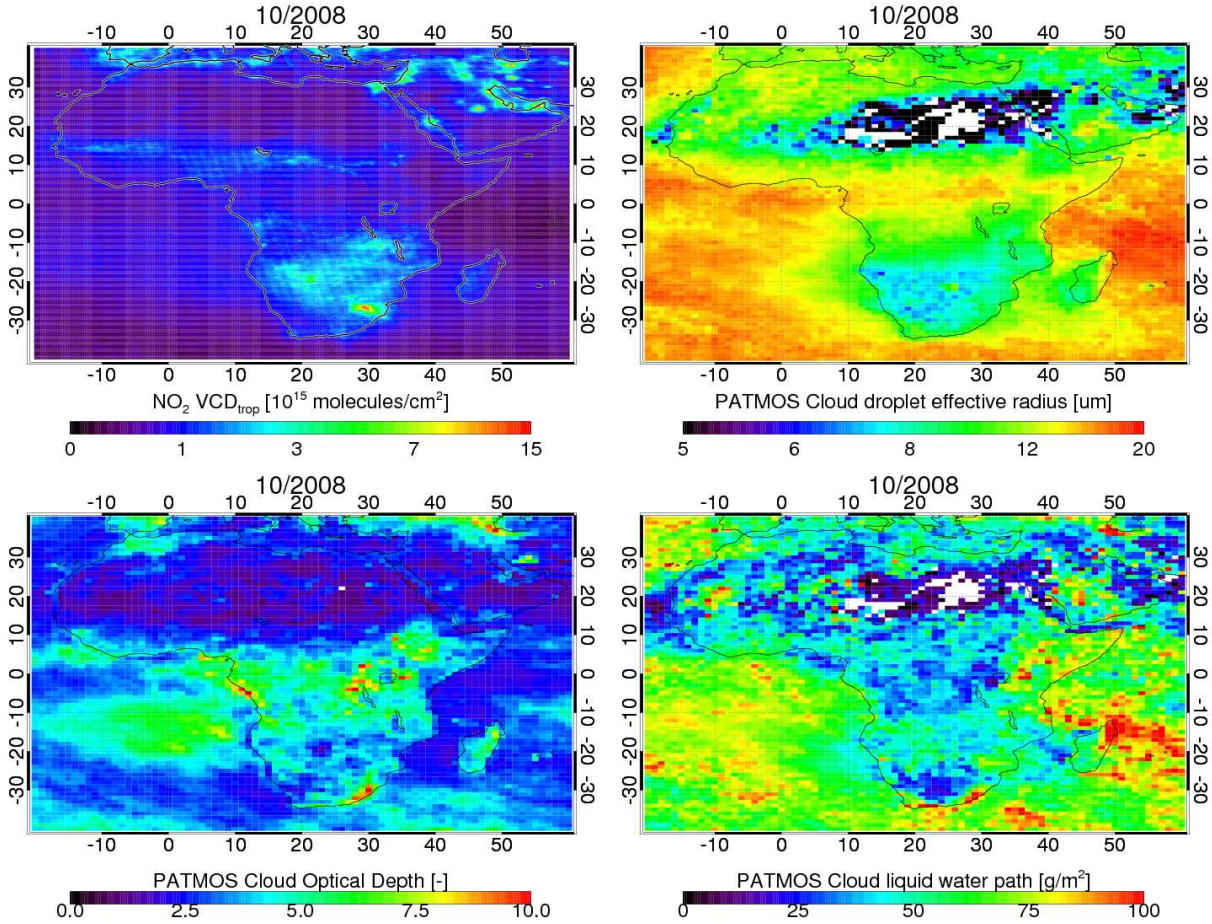

Figure 4: Top row: monthly means of OMI tropospheric NO_2 (left) and PATMOS-x r_e (right) over Africa for October 2008. Bottom row: monthly means of PATMOS-x COD (left) and LWP (right).

parameters derived from PATMOS-x observations. As can be seen in Figure 7 (a), there is no clear correlation between cloud optical depth and NO_2 over Europe and continental China, this in contrast to the China Sea where a stronger correlation is observed. Furthermore, panel (b) shows a small positive trend NO_2-r_e relation for European regions, which disagrees with the findings for the SEVIRI r_e that were presented in Figure 6.

Figure 7 (d) shows that over the biomass burning and the outflow areas in Africa the cloud droplet size consistently decreases with increasing NO_2, which suggests a clear manifestation of the AIE. However, the plots in panel (c) show that the COD decreases similarly with increasing NO_2, whereas according to the AIE the COD should increase due to the enhanced number of (smaller) droplets. It can not be excluded that the changes in cloud physical parameters over the selected regions in Africa are driven by climatology and that the relation between r_e and NO_2 is coincidental because biomass burning predominantly occurs in the dry season. The corresponding scatterdensity plots for the regions R_0–R_7, presented in Figure 8, show that below 2×10^{15}molecules/cm^2 increasing NO_2 columns correlate with smaller droplet diameters,

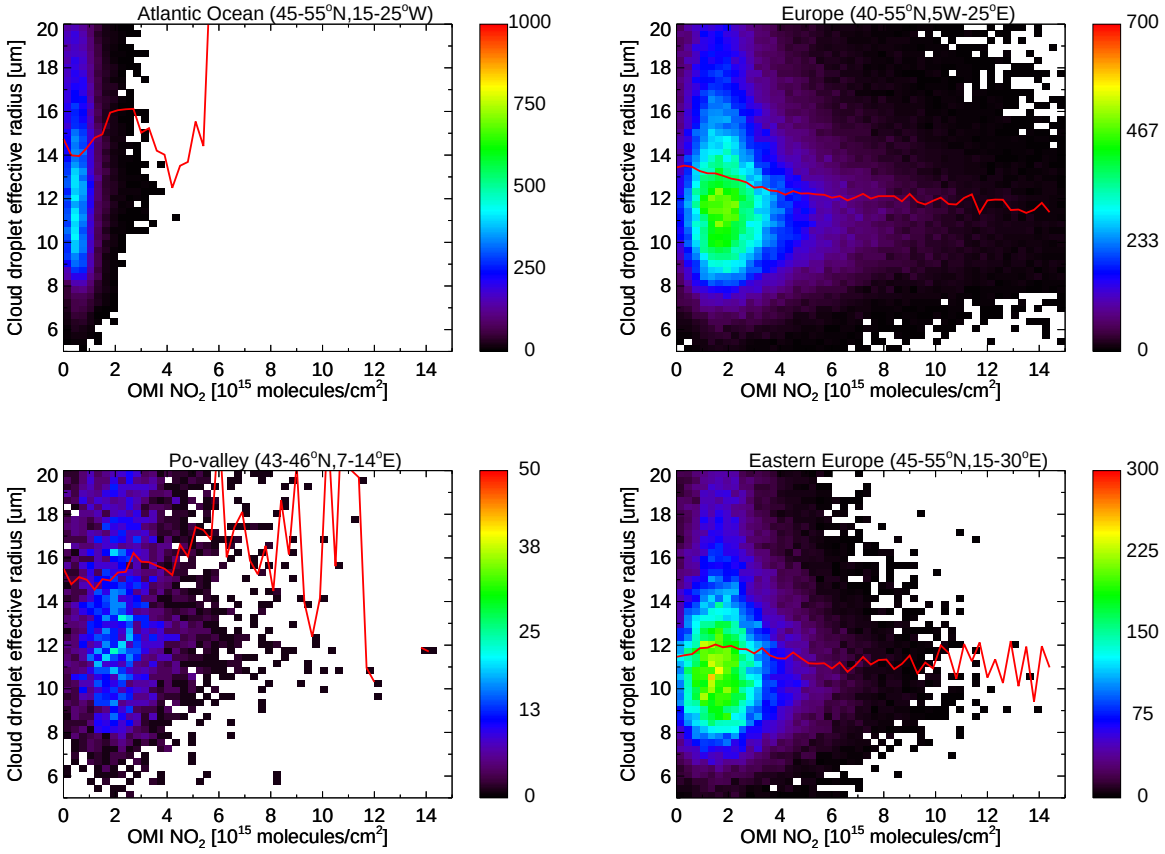

Figure 5: Scatterdensity plots showing the correlation between OMI tropospheric NO_2 and SEVIRI r_e for four regions in Europe for the period June–August 2008. The plots are based on the daily observations for each 0.25°x0.25° grid point in the region of interest. The color (linear scale) indicates the number of datapoints in each bin; the red trace represents the median of the r_e distribution for each NO_2 value.

but for larger NO_2 columns r_e basically remains constant.

3.2 PATMOS-x versus SEVIRI

The qualitative similarities between the spatial distributions of monthly averaged COD and r_e from SEVIRI and PATMOS-x were already mentioned in section 3.1 in a brief discussion of Figure 2. Yet, Figure 2 also clearly shows large quantitative differences in the COD values between both instruments, with SEVIRI COD being considerably higher than the COD values derived from PATMOS-x observations. In the processing of the SEVIRI data thin clouds (COD < 8) were excluded in order to obtain a data set that is better suited to investigate the possible correlation between NO_2 and r_e. As a consequence, the plots of the monthly averages of COD for SEVIRI and PATMOS-x can not be compared directly.
Histograms of the cloud droplet size distribution, presented in Figure 9, show good agreement

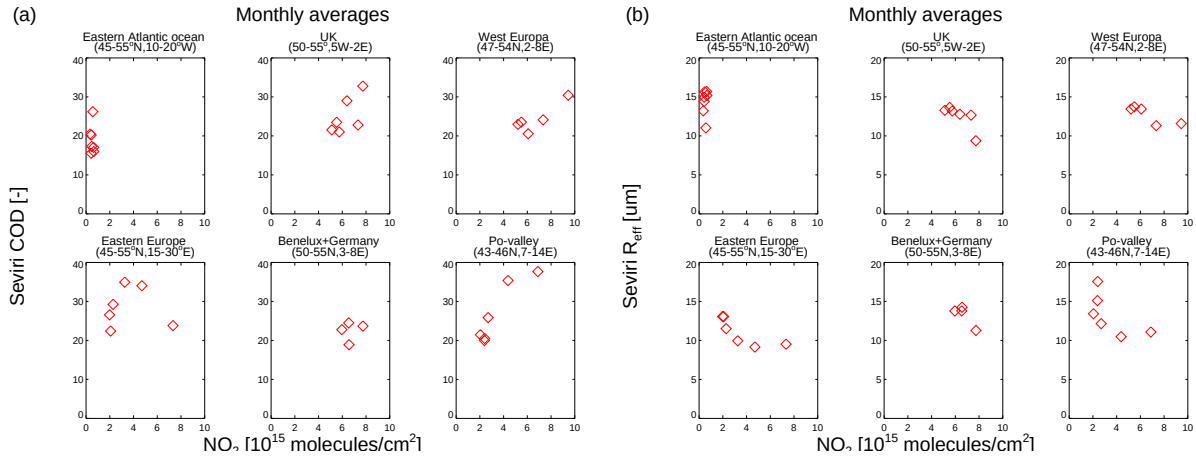

Figure 6: Scatterplots of regionally averaged monthly means of OMI tropospheric NO_2 versus cloud physical parameters retrieved from SEVIRI. (a) COD, (b) r_e. Observations from the period June 2008–May 2009 were used.

between SEVIRI and PATMOS-x. However, the scatterplots of r_e from both instruments, shown in the same Figure, show no strong correlation between both products but a certain amount of scatter around the 1:1 relation instead.
Again it is remarked that the discrepancies between r_e from SEVIRI and PATMOS-x may be attributable to differences in the data treatment while constructing the monthly averages.

3.3 Seasonal cycle

In Figure 10 the seasonal cycles of NO_2, AOT and cloud physical parameters are presented. This shows a clear seasonal dependence of the NO_2 load over its source regions with higher NO_2 columns in winter, resulting from the longer lifetime of NO_2 due to slower photochemistry. The fact that the seasonal dependence of NO_2 is mainly driven by its photochemistry complicates its application as a proxy for AOT throughout the year, as the seasonal cycle of NO_2 is opposite to the chemistry-driven seasonal variation of AOT. For a proper analysis of the temporal variability of NO_2 and AOT, the changing chemical and meteorological conditions should either be constant or be taken into account (if possible).
Over continental Europe, the SEVIRI-derived r_e is larger in summer than in winter, which is out of phase with the seasonal variation of NO_2, but in phase with the seasonal variation of AOT. The seasonal dependence of the cloud droplet size derived from PATMOS-x is not as profound as for SEVIRI, and if present, it is shifted in time with respect to SEVIRI.
The eastern Atlantic Ocean presents a reference for the climatological seasonal variation of the cloud droplet size at mid-latitudes in absence of pollution; in case of SEVIRI it ranges from 10–15 μm where the minimum values occur in winter while for the remainder of the year r_e is relatively constant. The seasonal variability derived from PATMOS-x data is approximately

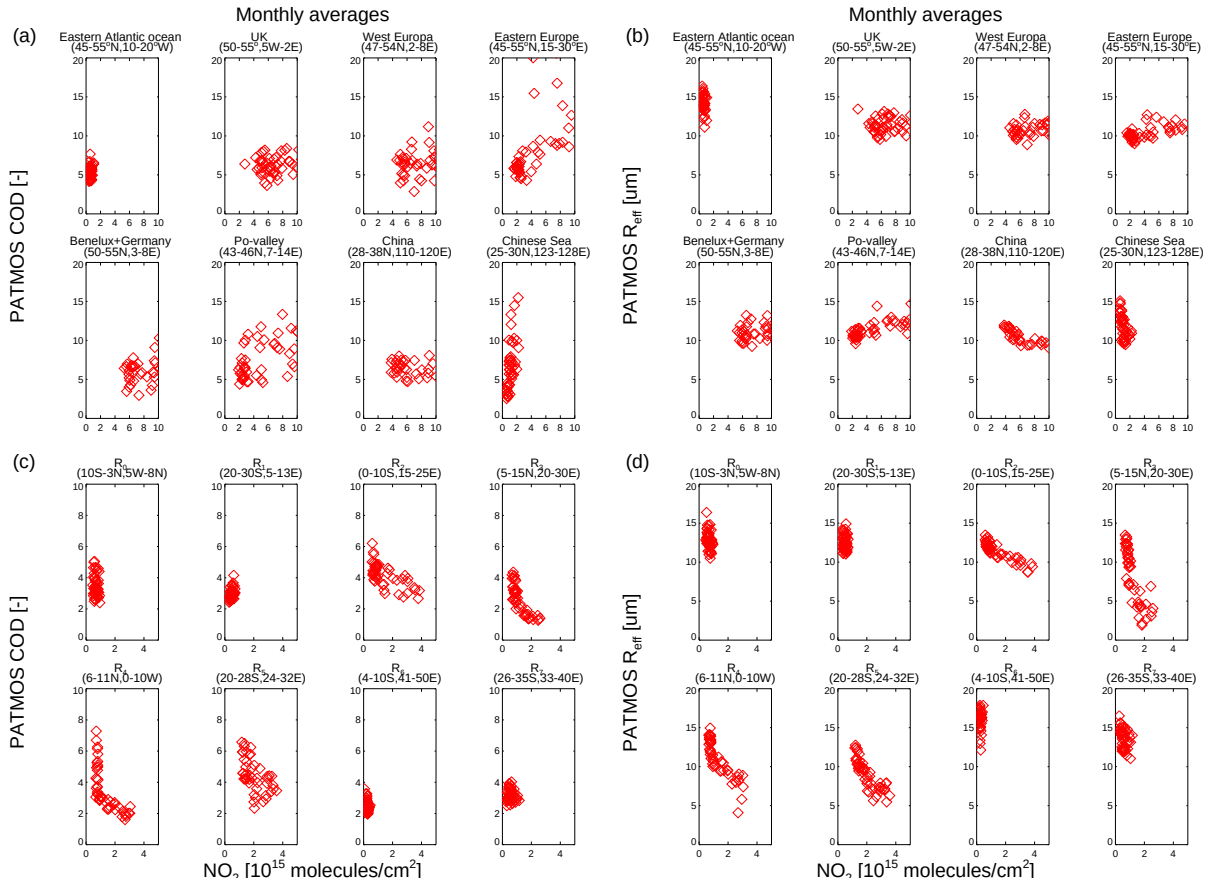

Figure 7: Scatterplots of collocated monthly averages of OMI tropospheric NO_2 versus cloud physical parameters retrieved from PATMOS-x. (a): COD versus NO_2 over Europe and China, and (c) over Africa. (b): r_e versus NO_2 over Europe and China, and (d) over Africa. Observations from the period 2005–2008 were used.

a factor two smaller (13–15 μm). Over the different seasons the range of r_e is roughly equal over continental Europe and over the ocean, although over the continent the cloud droplet size clearly peaks in summer, which reflects the influence of the continent on the seasonal cycle of r_e, both in terms of its phase and amplitude.

Over continental China the seasonal cycles of NO_2 and r_e are opposite, in the sense that in summer cloud droplet size is large when the NO_2 load is low. However, the same plot in Figure 10 also shows that the seasonal cycles of AOT and NO_2 are opposite, which in this case is inconsistent with the idea of NO_2 acting as a proxy for the aerosol load. The seasonal behavior of AOT and r_e do not seem correlated, but merely shifted in time with respect to each other. Therefore the question arises if the main driver behind the seasonal variability in cloud droplet size is climatology, for instance by the predominant direction of the wind (off-shore or on-shore).

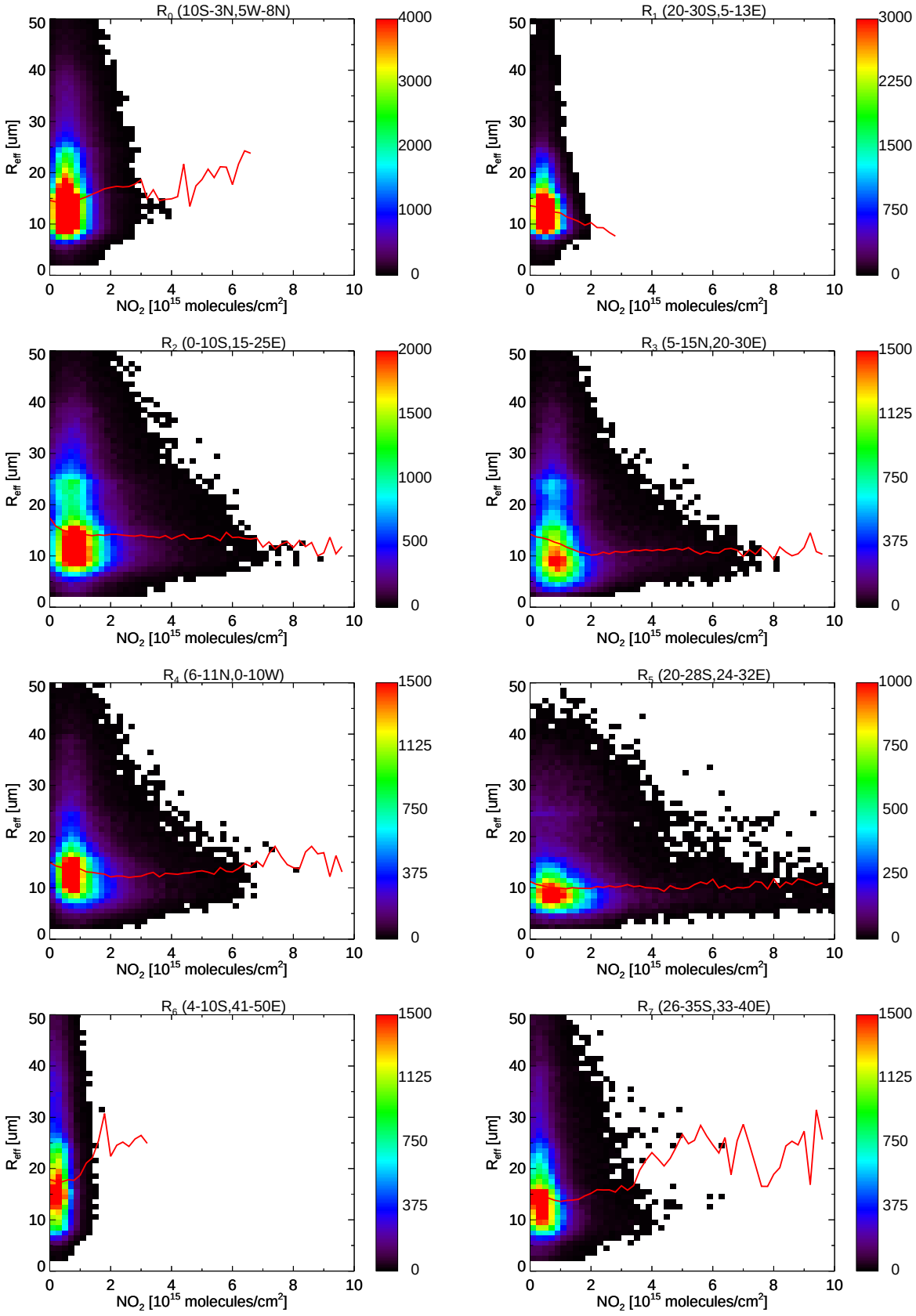

Figure 8: Scatterdensity plots showing the correlation between OMI tropospheric NO_2 and PATMOS-x r_e for eight regions in Africa for the period 2005–2008. The plots are based on the daily observations for each 0.25°x0.25° grid point in the region of interest. The color (linear scale) indicates the number of datapoints in each bin; the red trace represents the median of the r_e distribution for each NO_2 value.

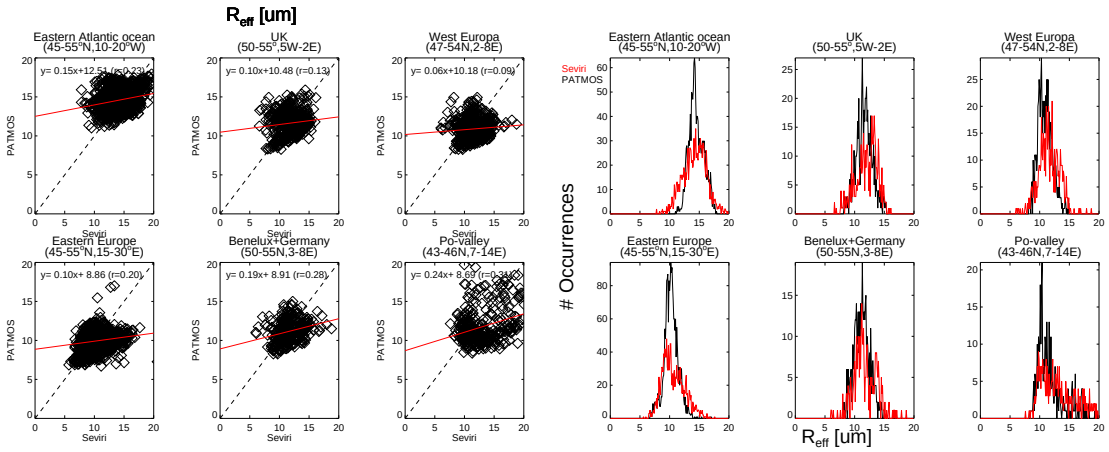

Figure 9: Comparison of cloud droplet size retrieved from SEVIRI and PATMOS-x over various regions in Europe. Shown are the value of the monthly averages for each grid point in the region of interest, measured between June 2008–May 2009. Columns 1–3: scatterplots, where the x-axis represents the SEVIRI data and the y-axis represents the PATMOS-x data. The dashed black line represents the 1:1 relation and the red line represents a linear fit to the data. Columns 4–6: histogram distributions of r_e for SEVIRI (red) and PATMOS-x (black).

Over the China Sea a remarkable anti-correlation in the seasonal cycles of AOT and r_e is observed, where the lowest value of the cloud droplet size occurs in spring, centered around April, when the AOT is highest. For the remainder of the year the AOT stays at its background level while r_e increases to follow its climatological cycle. The spring-time peak in AOT, and the accompanying minimum value of r_e, over the China Sea could be the result of outflow of polluted continental air transported by prevailing offshore winds, while during the rest of the year winds are predominantly onshore resulting in a lower (background) aerosol load. It is remarked that the observed anti-correlation in the seasonal dependence of NO_2 and r_e over China is consistent with the NO_2/r_e scatterplot presented in Figure 7. Similarly, the seasonal anti-correlation of AOT and cloud droplet size over the China Sea is consistent with the scatterplot of these parameters presented in Figure 11.

For Africa, the seasonal dependence of the cloud parameters COD and r_e is more profound over continental regions (R_2–R_5) than over the ocean. The most obvious correlation between NO_2/AOT and cloud droplet size occurs over central Africa (R_2). Over R_2 the seasonal dependencies of NO_2 and AOT are in phase, both peak in July/August when r_e has its lowest value. In the corresponding outflow area R_0, NO_2 is greatly reduced due to its limited lifetime by photochemical processing, but similar, though opposite, seasonal cycles are observed for AOT and r_e. The observed (anti)correlation between NO_2/AOT and r_e for the regions R_0 and R_2 is consistent with the scatterplots presented in Figures 7 and 11. Again, it can not be excluded that the correlation between NO_2/AOT and r_e results from climatology as the biomass burning usually is performed in the dry season, and because the decreased value of r_e does not lead to

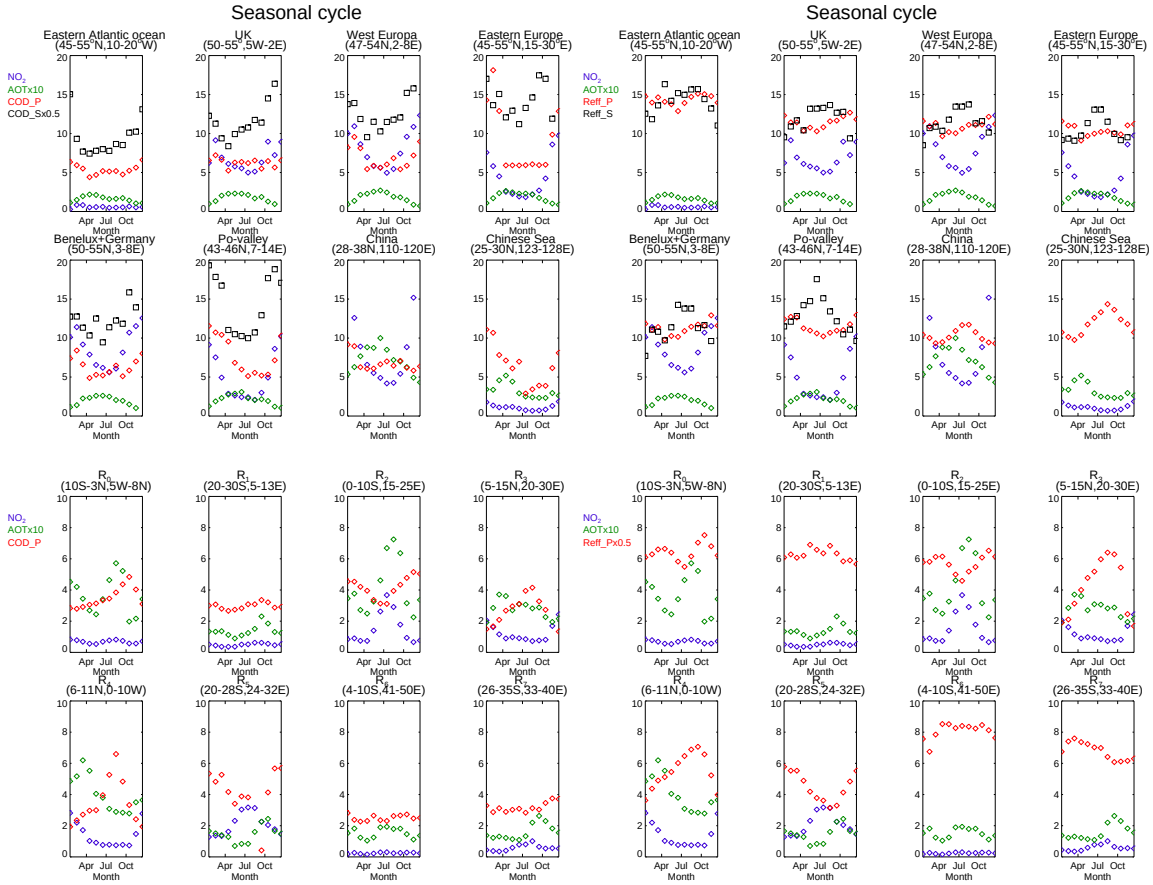

Figure 10: The seasonal cycle of tropospheric NO_2 (blue), AOT (green), and cloud parameters retrieved from PATMOS-x (red) and SEVIRI (black). In the columns on the left hand side the relevant cloud parameter is COD, in the right hand side columns, r_e. Each datapoint represents the average value of the monthly averaged datapoints in the region of interest for a specific month. The plots are based on measurement data from 2005–2008, for SEVIRI only measurements for June 2008–May 2009 are available. Multiplication factors are applied to AOT, COD and r_e, as indicated in the legend.

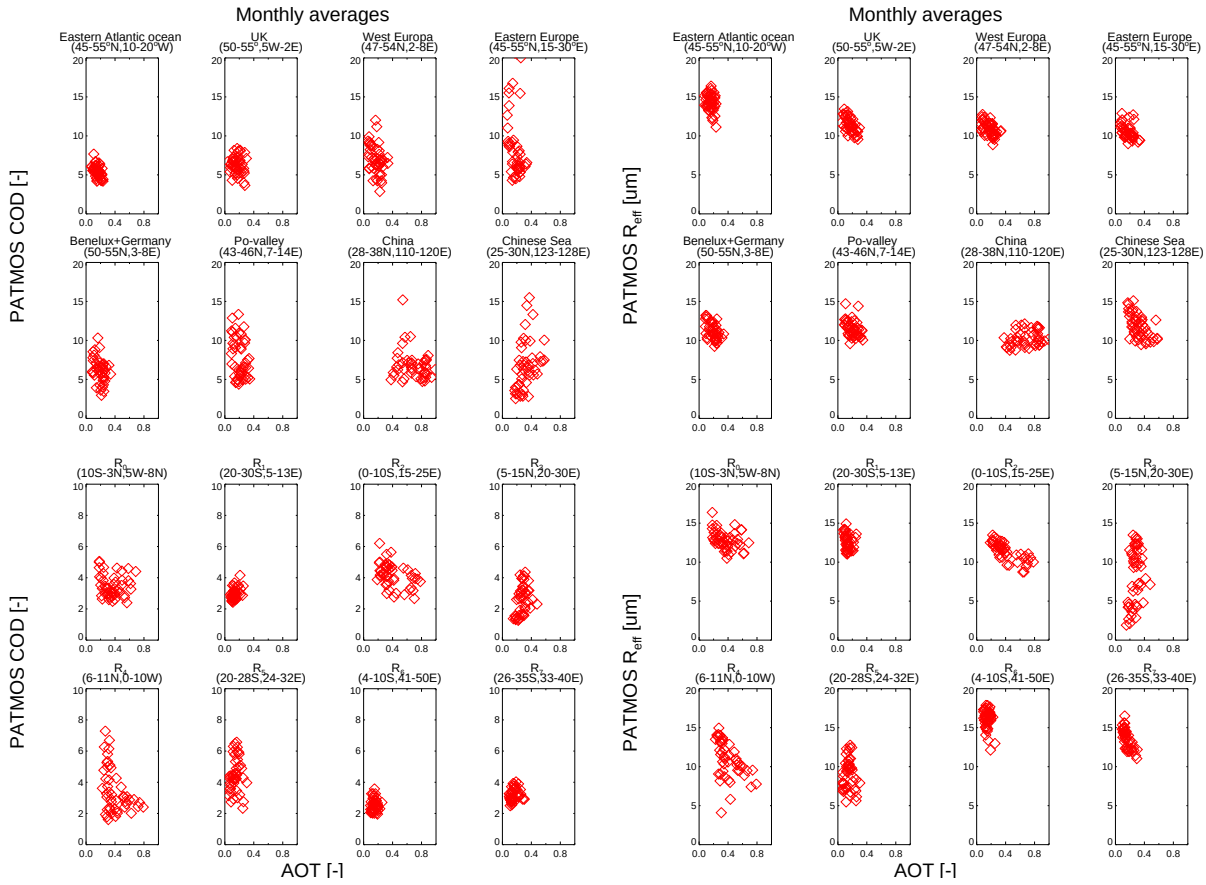

Figure 11: Scatterplots of collocated monthly averages of MODIS AOT versus cloud physical parameters retrieved from PATMOS-x. In the columns on the left hand side the relevant cloud parameter is COD, in the right hand side columns, r_e. Observations from the period 2005–2008 were used. The NO_2 columns are given in units of 10×10^{15} molecules/cm^2, the unit of r_e is μm, COD and AOT are unitless.

a corresponding increase in COD. Yet, the findings for regions R_0 and R_2 look very promising, and merits further investigation of individual events, where for example measurements by the spaceborne lidar CALIOP/CALIPSO can be used to determine the altitude of the aerosol layer. For the other continental regions (R_3–R_5) the plots in Figure 7 indicated a possible connection between NO_2 burden and r_e. Closer inspection of their respective seasonal dependencies in Figure 10 shows that the decrease of the cloud droplet size coincides with a sudden increase of NO_2, which marks the start of the biomass burning season. At the end of the biomass burning season, the decrease of NO_2 is accompanied by increasing droplet sizes. Yet, for regions R_3 and R_4 r_e continues to grow even after NO_2 has returned to its background level, which indicates the influence of climate on cloud droplet size and at the same time illustrates the complicating task of disentangling climatological influences from external factors.

4 Summary and outlook

In this project correlations between OMI tropospheric NO_2 columns and MODIS AOT, and the cloud physical parameters from SEVIRI and PATMOS-x were studied, with the purpose to investigate the possibility to use OMI NO_2 as a proxy for aerosol in observing the aerosol indirect effect. The approach followed in this study was to get a general overview of the statistical relationship between NO_2 and cloud parameters for cloudy scenes. This means that for the period of interest all available measurements from OMI, SEVIRI and PATMOS-x were used, rather than focusing on particular days or events. The analyses were performed on daily measurements and on monthly averages, for regions of interest over Europe and China (these harbor considerable sources of anthropogenic NO_2) and over major biomass burning areas in central and southern Africa with their associated outflow regions.

The results presented in this study show that over eastern Europe and the Po-valley higher NO_2 values correlate with smaller cloud droplets detected by SEVIRI. The decrease in r_e levels off at NO_2 column values exceeding 3×10^{15} molecules/cm^2. When comparing OMI NO_2 to cloud droplet size from PATMOS-x, this correlation between NO_2 and r_e is not found over Europe, but over China and over the biomass burning regions in Africa higher NO_2 values do correlate with smaller values of r_e. However, in case of Africa the correlation between NO_2 and smaller cloud droplets can also be driven by climatology, as the reduction of r_e correlates with smaller COD –opposite to what is expected for the AIE– and biomass burning predominantly occurs in the dry season.

The spatial distributions of cloud droplet size over Europe from SEVIRI and PATMOS-x are similar, although the PATMOS-x r_e values are more uniform over the continent, and smaller over the Mediterranean. Histogram distributions of r_e agree quite well between both instruments, but the correlation between r_e from both instruments is weak.

Evaluation of the temporal variation of NO_2, AOT, COD and r_e showed that over Europe SEVIRI r_e has a profound seasonal dependence that is opposite to the seasonal variation in NO_2, but in phase with the variability of AOT. The seasonal dependences of r_e from SEVIRI and PATMOS-x are not in phase over Europe. Over China high NO_2 loads correlate with small values of r_e, but the seasonal dependence of r_e is not consistent with the observed cycle in AOT. Over the China Sea, however, the seasonal cycles of AOT and r_e are consistent with AIE.

For Africa the seasonal cycles of NO_2 and AOT are in phase and opposite to the cycle of r_e, which is consistent with the AIE. The clearest example occurs over central Africa, although the period during which the cloud droplets are smallest coincides with a minimum in the COD, which is inconsistent with the AIE and indicates a connection with climatology instead.

For a follow-up of this project, it is suggested to focus on individual events rather than using the generalized statistical approach employed in this study. For a region such as Europe the inherent variability of cloud parameters due to the dynamic behavior of the (temperate) climate system it is challenging to isolate human induced changes from the background noise. For regions characterized by more steady weather, such as the (sub)tropics, a relation between NO_2 and the cloud droplet size is expected to be more straightforward to observe. Still it remains a

challenge to prove a causal relation between NO_2 and a change in cloud parameters. Therefore it is proposed to concentrate on individual events that are characterized by appropriate weather conditions for the AIE to occur, the presence of NO_2 and aerosol, to be determined from OMI and MODIS observations. Furthermore, additional observations from the spaceborne lidar CALIOP are needed to determine the altitude of the aerosol layer. The latter is necessary to establish that the aerosol and the cloud layer overlap so that one can be certain that the aerosols have interacted with the cloud. A comparable approach was followed by *Yuan et al.* (2011) to study the change of cloud physical properties in the plume of a Hawaiian volcano.

5 acknowledgements

Jürgen Fischer is thanked for providing the necessary workspace and computer infrastructure at the Institut für Weltraumwissenschaften at the Freie Universität Berlin to facilitate this project. Ralf Bennartz (University of Wisconsin) is thanked for fruitful discussions during the project, and Andi Walther (FUB & University of Wisconsin) generously provided the PATMOS-x data.

References

Avey, L., T. J. Garrett, and A. Stohl (2007), Evaluation of the aerosol indirect effect using satellite, tracer transport model, and aircraft data from the International Consortium for Atmospheric Research on Transport and Transformation, *J. Geophys. Res.*, *112*, D10S33, doi:10.1029/2006JD007581.

Bennartz, R. (2007), Global assessment of marine boundary layer cloud droplet number concentration from satellite, *J. Geophys. Res.*, *112*(D2), doi:10.1029/2006jd007547.

Bennartz, R., J. Fan, J. Rausch, L. R. Leung, and A. K. Heidinger (2011), Pollution from China increases cloud droplet number, suppresses rain over the East China Sea, *Geophys. Res. Lett.*, *38*(9), L09,704, doi:10.1029/2011gl047235.

Boersma, K. F., H. J. Eskes, and E. J. Brinksma (2004), Error analysis for tropospheric NO_2 retrieval from space, *J. Geophys. Res.*, *109*, D04311, doi:10.1029/2003JD003962.

Boersma, K. F., H. J. Eskes, J. P. Veefkind, E. J. Brinksma, R. J. van der A, M. Sneep, G. H. J. van den Oord, P. F. Levelt, P. Stammes, J. F. Gleason, and E. J. Bucsela (2007), Near-real time retrieval of tropospheric NO_2 from OMI, *Atmos. Chem. Phys.*, *7*, 2103–2118, doi:10.5194/acp-7-2103-2007.

Brenguier, J.-L., and R. Wood (2009), *Perturbed clouds in the climate system: Their Relationship to Energy Balance, Atmospheric Dynamics, and Precipitation*, chap. Observational strategies from the micro to meso scale, pp. 487–510, MIT Press, Cambridge, Massachusetts.

Edwards, D. P., L. K. Emmons, J. C. Gille, A. Chu, J. L. Attié, L. Giglio, S. W. Wood, J. Haywood, M. N. Deeter, S. T. Massie, D. C. Ziskin, and J. R. Drummond (2006), Satellite-observed pollution from Southern Hemisphere biomass burning, *J. Geophys. Res.*, *111*, D14312, doi:10.1029/2005JD006655.

IPCC (2007), *Climate Change 2007: The Physical Science Basis. Contribution of Working Group I to the Fourth Assessment Report of the Intergovernmental Panel on Climate Change*, 996 pp., Cambridge University Press, Cambridge, United Kingdom and New York, NY, USA.

Levelt, P. F., G. H. J. van den Oord, M. R. Dobber, A. Mälkki, H. Visser, J. de Vries, P. Stammes, J. O. V. Lundell, and H. Saari (2006), The Ozone Monitoring Instrument, *IEEE Trans. Geosci. Remote Sens.*, *44*(5), 1093–1101, doi:10.1109/TGRS.2006.872333.

Rausch, J., A. Heidinger, and R. Bennartz (2010), Regional assessment of microphysical properties of marine boundary layer cloud using the PATMOS-x dataset, *J. Geophys. Res.*, *115*(D23), D23,212, doi:10.1029/2010jd014468.

Roebeling, R. A., A. J. Feijt, and P. Stammes (2006), Cloud property retrievals for climate monitoring: Implications of differences between Spinning Enhanced Visible and Infrared Imager (SEVIRI) on METEOSAT-8 and Advanced Very High Resolution Radiometer (AVHRR) on NOAA-17, *J. Geophys. Res.*, *111*, D20210, doi:10.1029/2005JD006990.

Staudt, A. C., D. J. Jacob, J. A. Logan, D. Bachiochi, T. N. Krishnamurti, and N. Poisson (2002), Global chemical model analysis of biomass burning and lightning influences over the South Pacific in austral spring, *J. Geophys. Res.*, *107*(D14), 4200, doi:10.1029/2000JD000296.

Tanré, D., Y. J. Kaufman, M. Herman, and S. Mattoo (1997), Remote sensing of aerosol properties over oceans using the MODIS/EOS spectral radiances, *J. Geophys. Res.*, *102*, 16,971–16,988, doi:10.1029/96JD03437.

Twohy, C. H., P. A. Durkee, B. J. Huebert, and R. J. Charlson (1995), Effects of Aerosol Particles on the Microphysics of Coastal Stratiform Clouds, *J. Climate*, *8*(4), 773–783, doi:10.1175/1520-0442(1995)008<0773:EOAPOT>2.0.CO;2.

Twomey, S. (1974), Pollution and the planetary albedo, *Atmos. Environ.*, *8*(12), 1251–1256, doi:10.1016/0004-6981(74)90004-3.

Veefkind, J. P., K. F. Boersma, J. Wang, T. Kurosu, N. Krotkov, and P. F. Levelt (2011), Global analysis of the relation between aerosols and short-lived trace gases, *Atmos. Chem. Phys.*, *11*, 1255–1267, doi:10.5194/acp-11-1255-2011.

Yuan, T., L. A. Remer, and H. Yu (2011), Microphysical, macrophysical and radiative signatures of volcanic aerosols in trade wind cumulus observed by the A-train, *Atmos. Chem. Phys.*, *11*(14), 7119–7132, doi:10.5194/acp-11-7119-2011.